A multiscale volume of fluid method with self-consistent boundary conditions derived from molecular dynamics

Hanyi Liu[1], Jun Zhang[1,*], Paolo Capobianchi[2],

Matthew K. Borg[3], Yonghao Zhang[3], and Dongsheng Wen[1, 4]

[1]*School of Aeronautic Science and Engineering, Beihang University, Beijing 100191, China*

[2]*Department of Mechanical and Aerospace Engineering, University of Strathclyde,*

Glasgow G1 1XJ, United Kingdom

[3]*School of Engineering, University of Edinburgh, Edinburgh EH9 3FB, United Kingdom*

[4]*School of Chemical and Process Engineering, University of Leeds, Leeds LS2 9JT, United Kingdom*

Abstract

Molecular dynamics (MD) and volume of fluid (VOF) are powerful methods for the simulation of dynamic wetting at the nanoscale and macroscale, respectively, but the massive computational cost of MD and the sensitivity and uncertainty of boundary conditions in VOF limit their applications to other scales. In this work, we propose a multiscale simulation method by enhancing VOF simulations using self-consistent boundary conditions derived from MD. Specifically, the boundary conditions include a particular slip model based on the molecular kinetic theory for the three-phase contact line to account for the interfacial molecular physics, the classical Navier slip model for the remaining part of the liquid-solid interface, and a new source term supplemented to the momentum equation in VOF to replace the convectional dynamic contact angle model. Each slip model has been calibrated by the MD simulations. The simulation

---
* Corresponding author: jun.zhang@buaa.edu.cn

results demonstrate that with these new boundary conditions, the enhanced VOF simulations can provide consistent predictions with full MD simulations for the dynamic wetting of nanodroplets on both smooth and pillared surfaces, and its performance is better than those with other VOF models, especially for the pinning-depinning phenomenon. This multiscale simulation strategy is also proved to be capable of simulating dynamic wetting above the nanoscale, where the pure MD simulations are inaccessible due to the computational cost.

1. Introduction

When a droplet touches a solid substrate, it spreads spontaneously from an initial contact angle of 180° to its equilibrium value (θ_e). While the Young's equation [1] is generally recognized to describe the force balance at the equilibrium state of a wetted droplet, the prediction and modelling of a dynamic wetting process, which involves moving contact line and varying dynamic contact angle (θ_d), has still been controversial so far [2-4]. Dynamic wetting is ubiquitous in nature and of key importance in a variety of engineering applications. For instance, it is foundation of several industrial processes ranging from coatings [5] and pesticide spraying [6] at large scales, to microfluidic actuation [7] and nanoprinting [8] at micro and nano scales. Dynamic wetting is also crucial for droplet splashing [9], nucleate boiling [10], gyratory rebounding [11] and other droplet behaviours, which are all areas of increased research activity in recent years.

In terms of modelling dynamic wetting at the macroscale, various interfacial capturing/tracking techniques, including level-set [12], volume of fluid [13], and front tracking [14], have been developed and validated. In this work, we employ the volume of fluid (VOF) method as the continuum solver in view of its efficiency and extensive

use for the simulation of droplet dynamics [15-18]. It is well-known that the solution of the Navier-Stokes equations with no-slip boundary condition applied to the dynamic wetting problem brings a non-integrable stress singularity arising in the vicinity of the three-phase contact line [19]. Many theories have been proposed [20] to eliminate the stress singularity, such as the diffusive interface model [21], precursor film theory [22], surface tension gradient [23], and velocity slip models. In addition, a variety of dynamic contact angle (DCA) models have been developed based on the hydrodynamics, molecular kinetics, or empirical formulae to account for the variation of contact angle in the dynamic wetting process [24]. Note that velocity slip models and DCA models are usually used together, referred to as the boundary conditions in VOF [20]. It is difficult to evaluate which kind of boundary conditions are the best in VOF simulations of dynamic wetting at the macroscale, as various velocity slip and DCA models seem to be capable of giving satisfactory predictions [25], as long as the stress singularity at the contact line is circumvented. The reason for this is that the ratio of the contact line region (called "CL region" in this work) to the whole macro droplet is so small that the arising behaviours at the contact line is insignificant for the droplet dynamics as a whole. However, if the droplet size is down to sub-micro and nano scales, the role of boundary conditions becomes crucial for accurate predictions [26].

Molecular dynamics (MD) has been proved to be a power tool for probing the microscopic properties of wetting at the nanoscale. The implementation of MD is very simple, i.e., it solves Newton's equations of motion for each particle, and averages the properties of particles to obtain the macroscopic quantities of a system [27]. By performing MD simulations, researchers have found the underlying mechanism of forces at the contact line [28-30] and developed slip models for the continuum flow

simulations [31-34]. However, the application of MD to macro droplets is strictly limited by its expensive computational cost, despite the rapid developments of hardware during the past two decades. Considering the computational efficiency, a continuum simulation approach corroborated by appropriate microscopic models is a better choice when simulating droplets above the nanoscale. Nevertheless, the VOF method with standard boundary conditions developed for macroscale flows may be problematic for applications at the nano and sub-micron scales [35], where the particular contact line effects that relate to the interfacial molecular physics become dominant. Therefore, more suitable boundary conditions are highly required for the VOF methods to simulate the dynamic wetting of droplets with considerable small sizes.

Recently, some efforts have been put into the development of multiscale simulation methodology for the dynamic wetting problems [36], which is commonly carried out by means of domain decomposing [37] or hierarchical simulating [38]. Among them, we proposed a sequential multiscale strategy [26], i.e., the VOF simulations are performed with the boundary conditions resolved by MD. Specifically, the boundary conditions include the MKT slip for the three-phase contact line and the classical Navier slip for the remaining part of the liquid-solid interface, as well as the MKT DCA model that accounts for the contact angle changes. Our results demonstrated that capturing the particular slip behaviour at the contact line is crucial for the accurate prediction of dynamic wetting of nanodroplets. However, it should be noted that most of the DCA models, including the well-known Kistler's model [39], Shikhmurzaev's model [40], Kalliadasis's model [41], and the MKT DCA model, assume a relationship between the DCA and contact line velocity, while the contact line velocity is also an unknown quantity, which needs to be determined on-the-fly. Since the MKT slip model and the

4

MKT DCA model adopted in our previous work to calculate the contact line velocity and the instant DCA intrinsically come from one formula but just in different forms, they are actually implemented twice in one calculation step, which is still theoretically elusive and might result in accumulations of numerical errors.

To develop more self-consistent boundary conditions for the dynamic wetting simulations, the changes of DCA must be uncoupled from the slip models. In this work, we replace the MKT DCA model by including an additional source term into the VOF momentum equation, inspired by the recent work of Boelens and de Pablo [42]. The MKT slip model used in our previous work [26] is still kept to account for the particular slip behaviour at the CL region. We will demonstrate that this new strategy has the best performance among these methods in predicting the dynamic wetting process of nanodroplets, on both smooth and pillared surfaces.

The remainder of this paper is structured as follows. The simulation methodology and the corresponding theories are introduced in Section 2, including the standard VOF method, the self-consistent boundary conditions proposed in this work, the modelling and settings of MD simulations, and the implementation of the multiscale simulation methodology. Simulation results are presented in Section 3, including the MD-derived boundary conditions, the performance of the multiscale method in simulating dynamic wetting of nanodroplets, and the feasibility of extending this method to larger scales. Conclusions are provided in Section 4. Note that the standard VOF method in this paper refers to the VOF method with standard boundary conditions, i.e., with the Navier slip model for the whole liquid-solid interface and the DCA models for the variation of contact angle.

2. Theory and methodology

2.1 Volume of fluid method

2.1.1 The standard VOF method.

In this paper, all VOF simulations are performed using the modified OpenFOAM code [43]. The VOF method was first implemented in OpenFOAM as the interFoam solver [44], whose accuracy and efficiency have been assessed by Deshpande et al. for a variety of benchmark cases [45]. Numerous researchers have integrated new modules into the OpenFOAM code, benefiting from its open source nature, to simulate increasingly complex multiphase flows. In the present work, we develop new models and modify the original interFoam solver to make it efficient and accurate for the simulation of dynamic wetting at considerably small scales.

With the VOF method, the interface is captured by advecting a scalar function, α, which represents the volume fraction of one phase with respect to the total volume of fluid enclosed in one computational cell [13]. We assume that a computational cell fully occupied by the liquid or the gas phase has $\alpha = 1$ or $\alpha = 0$, respectively, and thus for a cell belonging to the interface there is $0 < \alpha < 1$. Accordingly, a transport equation for α [Eq. (1)] needs to be solved with the governing equations for the incompressible two-phase flows (continuity equation [Eq. (2)] and momentum equation [Eq. (3)]), that is,

$$\frac{\partial \alpha}{\partial t} + \nabla \cdot \left(\alpha \vec{U} \right) + \nabla \cdot \left(\alpha (1 - \alpha) \vec{U}_c \right) = 0, \tag{1}$$

$$\nabla \cdot \vec{U} = 0, \tag{2}$$

$$\frac{\partial \left(\rho \vec{U} \right)}{\partial t} + \nabla \cdot \left(\rho \vec{U} \vec{U} \right) = -\nabla p + \nabla \cdot \left(\mu \nabla \vec{U} \right) + \gamma k \nabla \alpha, \tag{3}$$

where t is the time, $\vec{U}$ is the velocity vector, ρ is the density, p is the pressure, μ

is the viscosity, and $\vec{U}_c$ is a "compressive", artificial velocity that is added to mitigate the smearing of the interface stemming from the presence of the divergence term, $\nabla \cdot (\alpha\vec{U})$, as the volume fraction is a steep function at the interface. The model is completed by defining the generic material property, χ, as a linear combination of the volume fraction, i.e. $\chi = \alpha\chi_l + (1 - \alpha)\chi_g$, where the subscripts l and g stand for "liquid" and "gas", respectively.

The classical Navier slip model, namely,

$$\vec{U}_s = l_s \frac{\partial \vec{U}}{\partial y}\Big|_{y=0}, \tag{4}$$

is commonly used as the boundary condition for the velocity field $\vec{U}$ to represent the slip behaviour at the solid-liquid interface, where l_s is the slip length. The last term on the right-hand side of Eq. (3) is the surface tension force defined by the continuum surface force (CSF) model [46]. That is, it is the product of the surface tension coefficient (γ), the gradient of the volume fraction ($\nabla\alpha$), and the curvature of interface (k). Note that the curvature of the interface is determined by the divergence of the unit normal vector of the interface ($\vec{n}$), i.e.,

$$k = -\nabla \cdot \vec{n}, \tag{5}$$

with the positive direction of $\vec{n}$ pointing from the lower volume fraction side to the larger one. This unit normal vector is approximated as

$$\vec{n} = \frac{\nabla\alpha}{|\nabla\alpha|}, \tag{6}$$

except at the computational cells that are next to the boundary walls and located in correspondence of the CL region (called "CL cells" in this work), where it is determined by the contact angle via

$$\vec{n} = \vec{n}_w\cos\theta_d + \vec{n}_t\sin\theta_d, \tag{7}$$

7

where $\vec{n}_w$ is the unit normal vector of the boundary wall, $\vec{n}_t$ is the unit vector tangential to the boundary wall and perpendicular to the contact line, and θ_d is the dynamic contact angle (DCA), as shown in Fig. (1). In this way, DCA virtually behaves as a geometric boundary condition, which determines the curvature of the interface (k) at the three-phase CL region and affects the dynamic wetting process accordingly. The correct value of DCA at each instant of time can be obtained by a DCA model, which prescribes the DCA as a function of time or the contact line velocity. Another more straightforward method that has similar effects as using DCA models is to explicitly include a force term into the momentum equation at the boundary cells [42,47,48]. This will be discussed in detail in Section 2.1.3.
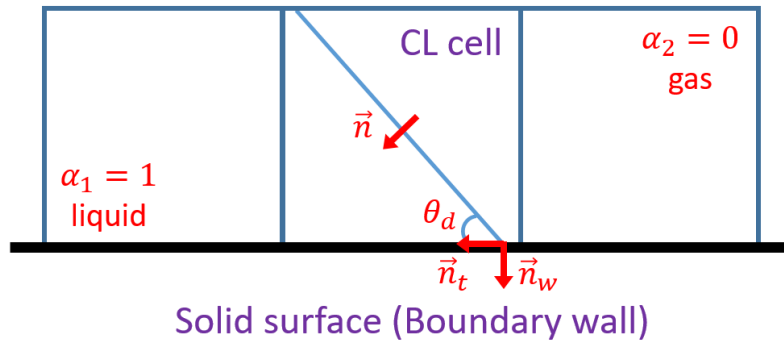
Fig. 1. Schematic of the unit vector and contact angle at the three-phase contact line.

2.1.2 Velocity slip boundary condition based on molecular kinetic theory.

It has been recognized that for an accurate simulation of dynamic wetting, not only the velocity slip behaviour for the common solid-liquid interface, as described by the Navier slip condition, plays a crucial role, but also the particular slip effect in the vicinity of the three-phase contact line is of vital importance [33]. As reported by our previous work [26], without considering the specific slip behaviour at the three-phase contact line, the model would fail on quantifying the speed of the dynamic wetting, unless an artificial large slip length is used in the Navier slip model. However, it should

8

be emphasized that the slip length is not an artificial parameter, but is related to the surface chemistry and solid-liquid interactions [49], whose value can be determined by MD simulations [50]. As a consequence, we follow our previous work [26] to account for the particular slip behaviour at the CL region by referring to the molecular kinetic theory (MKT) [51,52].

The principal hypothesis of the MKT model is that the dynamics of the three-phase contact line is determined by the statistical kinetics of molecular events occurring at the CL region. Two quantities, K^+ and K^-, are used to define the frequency of molecular displacements induced by thermal motions in the forward and backward directions at the CL region, respectively. When the droplet is at equilibrium, these two frequencies are approximately identical, that is,

$$K^+ = K^- = K_0 = \left(\frac{k_B T}{h}\right) \exp\left(-\frac{\Delta G^*}{N k_B T}\right), \tag{8}$$

where k_B is the Boltzmann constant, h is the Planck constant, T is the absolute temperature, N is the Avogadro number, and ΔG^* is the molar activation free energy of wetting. In this case, the contact line is stationary. However, once the instantaneous DCA (θ_d) deviates from its equilibrium value (θ_e), a localized shear stress, which is referred to the uncompensated or unbalanced Young's stress, would be generated at the three-phase region, that is,

$$w = \gamma(\cos\theta_e - \cos\theta_d). \tag{9}$$

This uncompensated stress alters the activation energy barrier of molecular displacements in two directions, and changes the displacement frequencies as follows,

$$K^\pm = \left(\frac{k_B T}{h}\right) \exp\left(-\frac{\Delta G^*}{N k_B T} \pm \frac{w}{2n k_B T}\right), \tag{10}$$

which results in the movement of the contact line with a velocity of

$$U_{CL} = \lambda(K^+ - K^-). \tag{11}$$

Defining two dimensionless constants $B = (2nk_BT)/\gamma$ and $C = (2\mu_l\lambda K_0)/\gamma$, Eq. (11) can be written as

$$U_{CL} = \frac{C\gamma}{\mu_l}\sinh\frac{(\cos\theta_e - \cos\theta_d)}{B}, \tag{12}$$

where γ is the surface tension coefficient, n is the number of adsorption sites per unit area on the solid surface, λ is the characteristic length of molecular displacement, and μ_l is the dynamic viscosity of the liquid. Equation (12) will be employed as the velocity slip boundary condition at the three-phase CL region in VOF, with the values of B and C determined by our MD simulations presented below.

2.1.3 Replacing the DCA model by a source term in the momentum equation.

Alternatively, Equation (12) can be reformulated in terms of the dependence of DCA on the contact line velocity, namely,

$$\theta_d = \arccos\left(\cos\theta_e - B\text{arcsinh}\frac{Ca}{C}\right), \tag{13}$$

where $Ca = (\mu_lU_{CL})/\gamma$ is the capillary number. In our previous work [26], we directly implemented Eq. (12) (the MKT slip model) and Eq. (13) (the MKT DCA model) as the boundary conditions for the slip velocity and the contact angle, respectively. To avoid the intertwining of the calculations of the contact line velocity and DCA, and to improve the self-consistency of boundary conditions as explained in Section 1, in this paper, we dismiss the DCA model and employ an alternative way to account for the changes of DCA during dynamic wetting.

According to the MKT theory, the driving force for the movement of contact line is the uncompensated Young's stress, which is composed of the dynamic effect $f_d = \gamma\cos\theta_d$ and the equilibrium effect $f_e = \gamma\cos\theta_e$. As shown in Fig. 2, in the previous

method, these two effects are incorporated into the MKT DCA model, which is used as a boundary condition to modify the interfacial curvature (k) at the boundary cells and hence the source term $\gamma k \nabla \alpha$ in the momentum equation. Conversely, if the interfacial curvature (k) is not corrected by the DCA model, but is directly determined by the instant flow field, the resulting source term $\gamma k \nabla \alpha$ accounts for dynamic effects without considering the equilibrium effect. Therefore, a promising way to replace the DCA model is to retain the original source term for the dynamic effect and adding a new source term to account for the equilibrium effect in the momentum equation. Note that the additional source term is only accounted for the CL cells. At the liquid-gas interfacial cells away from the solid wall, only the original source term $\gamma k \nabla \alpha$ is used to describe the surface tension exerted on the liquid-gas interface.
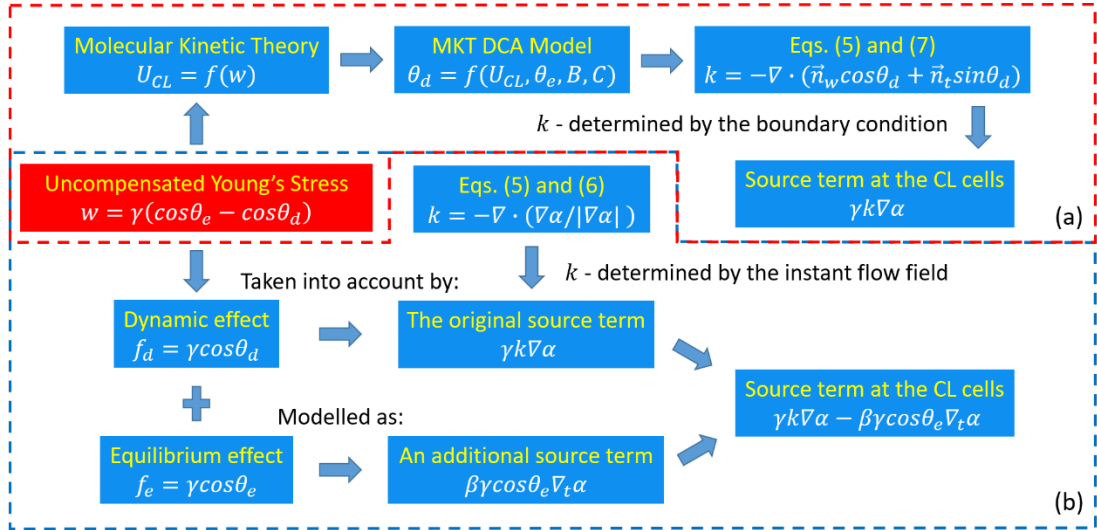
Fig. 2. Considering the effect of the uncompensated Young's stress in the VOF method: (a) using the MKT DCA model as a boundary condition; (b) keeping the original source term for the dynamic effect and modelling the equilibrium effect using a new source term in the momentum equation.

The modelling approach of the equilibrium effect (f_e) is analogous to that of the CSF model. We refer the readers to the recent paper published by Boelens and de Pablo [42] for a detailed theoretical derivation, while here we provide a brief account of its

implementation in the interFoam solver. To this end, we note that $\vec{f}_e$ is a line force

exerted on the three-phase contact line, namely,

$$\vec{f}_e(\vec{x}_L) = \gamma cos\theta_e \vec{n}_t(\vec{x}_L), \tag{14}$$

where $\vec{x}_L$ is position vector of the point forming the contact line. Since the contact line

is not tracked explicitly in VOF methods and its exact location is unknown, we need to

convert $\vec{f}_e$ to an equivalent surface force, $\vec{f}_{eA}$, exerted on the diffuse interface, that is,

$$\lim_{h \to 0} \iint_A \vec{f}_{eA}(\vec{r}) \, d\vec{r} = \int_L \vec{f}_e(\vec{x}_L) dL, \tag{15}$$

where $\vec{r}$ is the position vector of the points located in the solid wall plane lying inside

the diffuse CL region, and h is the width (or thickness) of this region. On the other

hand, through adopting the delta function, $\delta(\vec{r} - \vec{x}_L)$, the integral of $\vec{f}_e$ over the

contact line can be converted to a surface integral over the diffuse CL region, as

indicated below,

$$\int_L \vec{f}_e(\vec{x}_L) dL = \iint_A \vec{f}_e(\vec{r}) \cdot \delta(\vec{r} - \vec{x}_L) \, d\vec{r}, \tag{16}$$

where the delta function is defined as

$$\begin{cases} \delta(\vec{r} - \vec{x}_L) = 0, (\vec{r} \neq \vec{x}_L) \\ \iint_A \delta(\vec{r} - \vec{x}_L) \, d\vec{r} = 1 \end{cases}. \tag{17}$$

Comparing Eqs. (15) and (16), the surface force $\vec{f}_{eA}$ can be identified as

$$\lim_{h \to 0} \vec{f}_{eA}(\vec{r}) = \gamma cos\theta_e \vec{n}_t(\vec{r}) \cdot \delta(\vec{r} - \vec{x}_L). \tag{18}$$

Supposing the liquid-gas interface is sharp (instead of diffuse), the liquid volume

fraction (α) field can be expressed using a discontinuous function as follows,

$$\lim_{h \to 0} \alpha(\vec{r}) = \begin{cases} 1 & (\vec{r} < \vec{x}_L) \\ 0.5 & (\vec{r} = \vec{x}_L), \\ 0 & (\vec{r} > \vec{x}_L) \end{cases} \tag{19}$$

and thus the gradient of α along the plane of the boundary wall is

$$\lim_{h \to 0} \nabla_t \alpha(\vec{r}) = (1 - 0)\vec{n}_t(\vec{r}) \cdot \delta(\vec{r} - \vec{x}_L). \tag{20}$$

Comparing Eqs. (18) and (20), the delta function is to be substituted by the two-dimensional gradient of α, namely,

$$\vec{f}_{eA} = \gamma cos\theta_e \nabla_t \alpha, \tag{21}$$

where $\nabla_t \alpha$ can be easily computed through the interFoam solver, implemented as

$$\nabla_t \alpha = \nabla\alpha - (\nabla\alpha \cdot \vec{n}_w)\vec{n}_w. \tag{22}$$

The last step is to convert $\vec{f}_{eA}$ to an equivalent body force $\vec{f}_{eV}$ exerted on the CL cells, so that it can be incorporated into the momentum equation as a source term, that is,

$$\vec{f}_{eV}\Delta V_{CL} = \vec{f}_{eA}\Delta A_{CL}, \tag{23}$$

where ΔV_{CL} is the volume of a CL cell, and ΔA_{CL} is the area of its face that belongs to the boundary wall. Note that ΔA_{CL} and ΔV_{CL} are mesh properties that can be directly accessed in the interFoam solver. Consequently, the momentum equation is modified to

$$\frac{\partial(\rho\vec{U})}{\partial t} + \nabla \cdot (\rho\vec{U}\vec{U}) = -\nabla p + \nabla \cdot (\mu\nabla\vec{U}) + \gamma k\nabla\alpha - \beta\gamma cos\theta_e \nabla_t\alpha, \tag{24}$$

with the prefactor

$$\beta = s \cdot g(\alpha) \cdot (\Delta A_{CL}/\Delta V_{CL}), \tag{25}$$

in which the coefficient s is an on-off switch to localize the new source term activated only at the CL cells, that is, $s = 1$ for CL cells and $s = 0$ for the other ones. The modification function $g(\alpha)$ is necessary when the grid resolution is low, and this is further discussed in the Supplementary Material [53].

As the last two terms on the right-hand side of Eq. (24) represent the dynamic and equilibrium effect of the uncompensated Young's stress, it is expected that the contact angle of droplet automatically changes in the process of dynamic wetting, relying on the induced flow field rather than the prescribed function of any DCA models.

Accordingly, the present method is uncoupled with the velocity slip model for the three-phase contact line, and this is the key advantage in comparison with our previous method for dynamic wetting [26].

2.2 Molecular dynamics

We build two MD systems to simulate the dynamic wetting of water droplets and the Couette flow of water. The former is to provide a benchmark result at the nanoscale for the evaluation of different VOF models and to determine the values of the parameters B and C in the MKT slip model, while the latter is to determine the value of the slip length in the Navier slip model. All the MD simulations are performed using the Large-scale Atomic/Molecular Massively Parallel Simulator (LAMMPS) [54], and the results are visualized by the Open Visualization Tool (OVITO) [55].

In the dynamic wetting cases, four nanodroplets of different sizes with the initial radius (r_0) of 25.6 Å, 39.1 Å, 55.8 Å, and 72.5 Å, consisting of 2342, 8337, 24233, and 53152 water molecules, respectively, have been considered. The solid surfaces are composed of copper-like atoms, which are FCC structured with the lattice constant $L_c=$ 3.615 Å. Two different surface morphology are simulated, as shown in Fig. 3 (a) and (b), with one molecularly smooth and another decorated with concentric annular pillars, whose thickness, spacing and height are $3L_c$, $3L_c$ and L_c, respectively. Each nanodroplet first experiences sufficient relaxation using the Nosé-Hoover thermostat at 300 K to make its potential energy reach a stable minimum [56]. Subsequently, the droplet is placed right above the solid surface in such a way that the distance between the closest oxygen and the solid atom is 2 Å. Each case is run in the microcanonical ensemble for 1.05 million steps, with a computational time step of 0.002 ps.

In the Couette flow cases, 6402 water molecules are confined between two parallel horizontal solid plates at a distance of 120 Å, as shown in Fig. 3(c). The upper plate keeps moving at a constant velocity and the bottom one remains stationary. Periodic boundary conditions are assumed for the directions parallel to the two plates. After the system reaches a steady state, the streamwise velocities are measured in layers distributed along the direction normal to the solid surface, and then the slip length can be determined straightforwardly according to the Navier slip model.
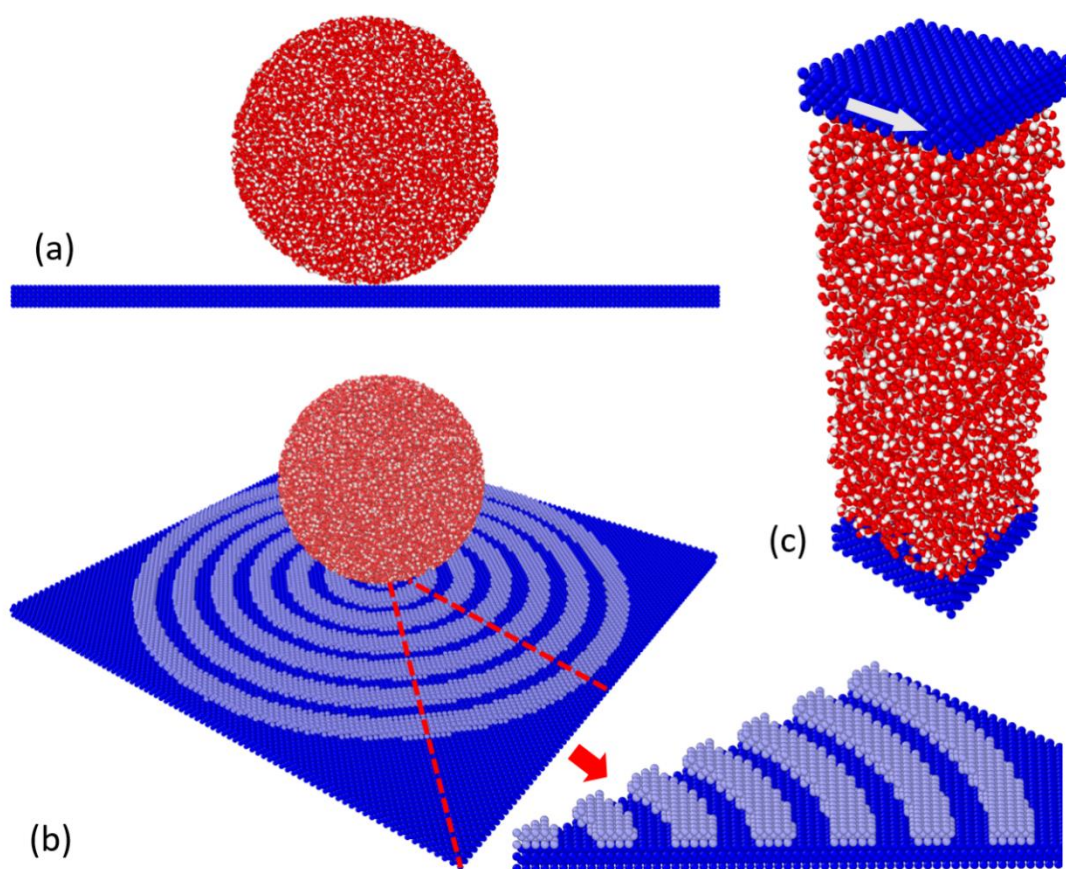
Fig. 3. Snapshots of the initial MD system in different cases. The white, red and blue particles represent oxygen, hydrogen, and solid atoms, respectively. (a) The smooth surface case from the front view. (b) The pillared surface case from the perspective view, and an enlarged view of one eighth of the pillared surface. Note that the substrate (dark blue) and pillars (light blue) consist of the same type of atoms, and the different colouring is just used for a clear distinction. (c) The Couette flow case from the perspective view.

Water molecules in all cases are simulated using the TIP4P/2005 model, which is

an acknowledged rigid planar model consisting of one Lennard-Jones center (the oxygen atom) and three point charges (two hydrogen atoms and one virtual M point) [57]. The interaction between any two water molecules i and j is represented by a van der Waals term and a Coulomb term, namely,

$$U_{ij} = 4\epsilon_O \left[\left(\frac{\sigma_O}{r_{ij}} \right)^{12} - \left(\frac{\sigma_O}{r_{ij}} \right)^6 \right] + \frac{1}{4\pi\varepsilon_0} \sum_{a,b} \frac{q_a q_b}{r_{ab}}, \qquad (26)$$

where r_{ij} is the distance between the Lennard-Jones centers, and a and b stand for the charged sites. Other parameters appearing in Eq. (26), including the Lennard-Jones parameters of oxygen, the charges of hydrogen and the massless site M, and the permittivity of vacuum, are listed in Table 1. The SHAKE algorithm [58] is applied to ensure that the oxygen-hydrogen bond length is 0.9572 Å and the H-O-H bond angle is fixed as 104.52°. The interactions between two solid atoms are described using a Lennard-Jones potential with the parameters ϵ_s=0.4093 eV and σ_s=2.338 Å [59]. The interactions between water molecules and solid atoms are also described by the Lennard-Jones potential, and the parameters are determined by the Lorentz-Berthelot mixing rule, i.e., $\sigma_{s,O} = (\sigma_s + \sigma_o)/2$ and $\epsilon_{s,O} = k_\epsilon \sqrt{\epsilon_s \epsilon_o}$, where k_ϵ is a scaling parameter to tune the interaction strength. We set k_ϵ=0.33 and 0.25 in this work to simulate two kinds of surfaces, corresponding to the static contact angle of 34.5° and 66.0°, respectively.

Table 1. Parameters of the TIP4P/2005 model [57]

ϵ_O (eV)	σ_O (Å)	q_O(e)	q_H(e)	q_M(e)	ε_0 (F/m)
8.0312×10^{-3}	3.1589	0	0.5564	-1.1128	8.8542×10^{-12}

2.3 Multiscale simulation methodology

In summary, the multiscale simulation methodology in this work is implemented as

follows:

(1) The MKT slip and the Navier slip models are implemented into the VOF method as the boundary conditions for the CL regions and for the remaining part of the solid-liquid interface, respectively, as shown in Fig. (4).

(2) Molecular dynamics simulations are performed to determine the parameters (B and C) in the MKT slip model and the slip length in the Navier slip model.

(3) A new source term, $\beta\gamma cos\theta_e \nabla_t \alpha$, is added to the momentum equation in VOF and activated at the CL cells. Together with the surface tension force term, $\gamma k\nabla\alpha$, the change of DCA is automatically considered.

$$\frac{\partial(\rho\vec{U})}{\partial t} + \nabla \cdot (\rho\vec{U}\vec{U}) = -\nabla p + \nabla \cdot (\mu\nabla\vec{U}) + \gamma k\nabla\alpha - \beta\gamma cos\theta_e \nabla_t\alpha$$

CL cells

MKT slip

Navier slip

CL cells

MKT slip
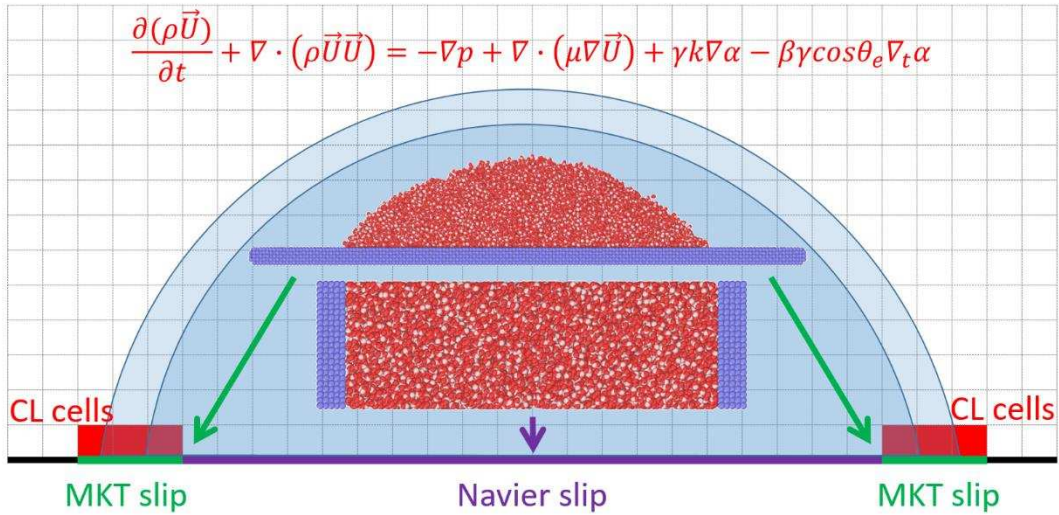
Fig. 4. Schematic of the multiscale simulation method. The region between two semicircles represents the liquid-gas interface captured by the VOF method.

3. Results

3.1 Molecular dynamics derived boundary conditions for VOF.

We first determine the constants in the MKT model and the slip length in the Navier slip model through MD simulations of dynamic wetting and Couette flow, respectively. For each dynamic wetting case, we divide the whole simulation domain into two-dimensional bins and determine the density distribution of a droplet by

counting the number of water molecules contained in each bin. The liquid-gas interface is defined by the locations of bins where the density is half the value inside the droplet [60]. Fig. 5(a) shows the temporal evolution of the liquid-gas interface for the droplet with an initial radius of 55.8 Å. By making a linear fit through the points of the liquid-gas interface in the range of 6 ~ 15 Å above the solid surface, i.e., the line denoted as Line (1) shown in Fig. 5(b), we determine the DCA corresponding to each instant of time. When the wetting process is sufficiently developed, the equilibrium contact angle on different surfaces can be measured. Our MD results predict $\theta_e = 34.5°$ for k_ϵ=0.33 and $\theta_e = 66.0°$ for k_ϵ=0.28.

As shown in Fig. 5(b), to avoid an overestimation of the base radius (r_b), we evaluate it through the distance from the droplet center to the intersection of Line (2) instead of Line (1) with the solid surfaces, where Line (2) is defined as a vertical line that intersects with Line (1) at the distance of 4 Å above the solid surface. Figure 5(c) presents the temporal evolution of the base radius during wetting. Note that the radius and time are normalized as $r^* = r_b/r_0$ and $t^* = t/\sqrt{\rho_l r_0{}^3/\gamma}$, respectively. We fit r^* as a ratio of polynomial functions of t^*, namely,

$$r^*_{fit} = \frac{\sum_{k=0}^{k_{max}} a_k (t^*)^k}{1 + \sum_{k=1}^{k_{max}} b_k (t^*)^k},\tag{27}$$

where a_k and b_k are free parameters to be adjusted, and k_{max} is the order of the best polynomial that minimizes the error but still gives r^*_{fit} as a concave increasing function [61], and then the Capillary number can be calculated via

$$Ca = \frac{\mu_l U_{CL}}{\gamma} = \frac{\mu_l}{\sqrt{\gamma \rho_l r_0}} \frac{dr^*_{fit}}{dt^*}.\tag{28}$$

Finally, the values of parameter B and C in the MKT slip model are determined by fitting the MD results of θ_e, θ_d and Ca to Eq. (13), as shown in Fig. 5(d).
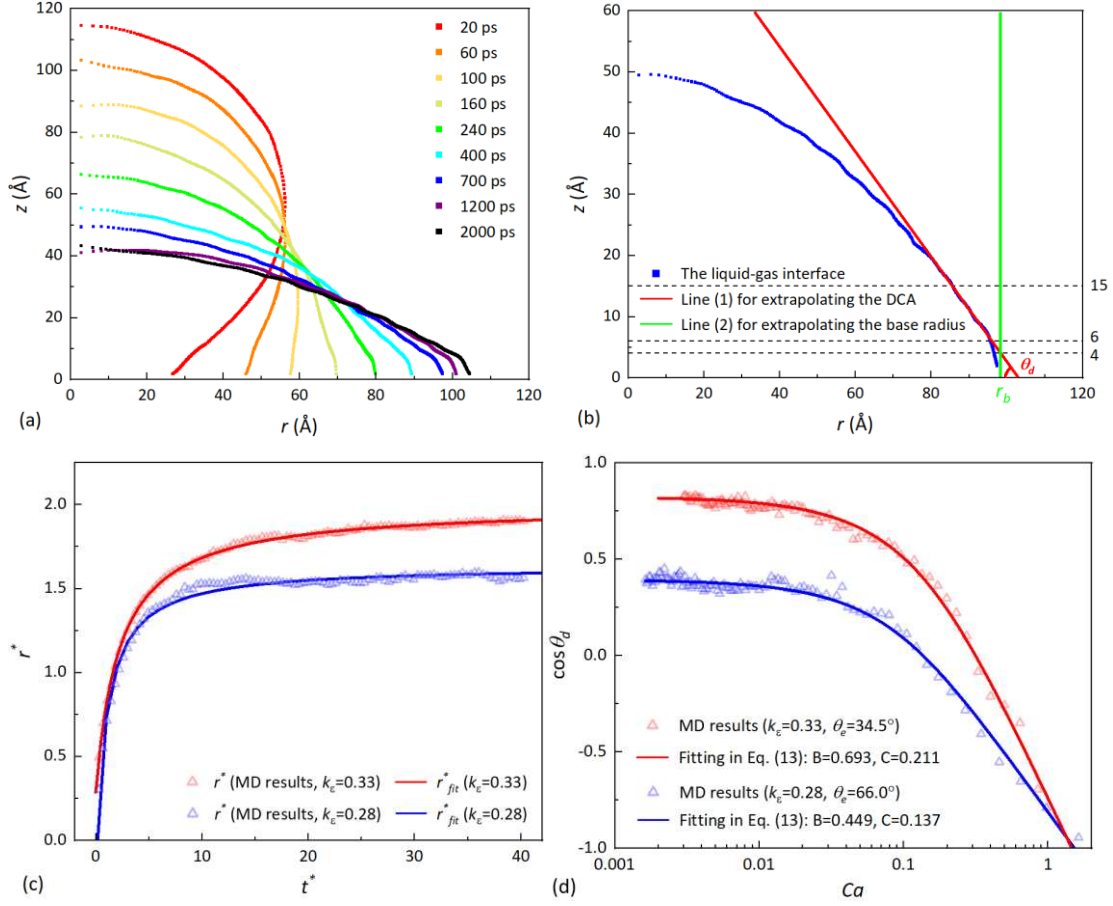
Fig. 5. (a) Temporal evolution of the liquid-gas interface during the wetting process of a droplet (r_0=55.8 Å) on the solid surface (k_ϵ=0.33). (b) Schematic of evaluating the DCA and base radius of a wetting droplet (t=700 ps). (c) Temporal evolution of the normalized base radius of the droplet (r_0=55.8 Å) and its fitting curve. (d) Extrapolation of the constant B and C in the MKT slip model by fitting MD results to Eq. (13).

For the Couette flow cases, we divide the computational domain between two plates into 30 layers, and calculate the average velocity of water molecules in each layer. The slip length (l_s) can be determined by solving Eq. (4) with MD data, and the results give l_s=3.30 Å for k_ϵ=0.33 and l_s=4.35 Å for k_ϵ=0.28.

3.2 Multiscale simulation of dynamic wetting of nanodroplets.

We first compare the results obtained by different VOF models with those obtained by full MD simulations to evaluate the performance of the multiscale method in the simulation of dynamic wetting at the nanoscale. To this end, five distinct VOF solvers

are implemented with identical initial flow fields but under different boundary conditions for the velocity slip and contact angle, as presented in Table 2. Specifically, Solver 1 denotes the native interFoam solver in OpenFOAM, without any velocity slip model and with a constant (static) contact angle; Solver 2 corresponds to the standard VOF method, with the Navier slip model for the whole liquid-solid interface and a DCA model for the variation of contact angle, and specifically, we use the MKT DCA model for comparison with Solver 3; Solver 3 is identical to the one employed in our previous work [26], where the MKT slip model is used for the CL region and the Navier slip model is used for the remaining liquid-solid interface, and the MKT DCA model is used for the variation of contact angle; Solver 4 is identical to the one employed in reference [42], with the Navier slip model for the whole liquid-solid interface and a modified source term added in the momentum equation; Solver 5 is the newest one proposed in this work, where the velocity slip model is the same as in Solver 3, while a modified source term analogous to Solver 4 is added in the momentum equation to replace the DCA model.

Table 2. Boundary conditions of different VOF solvers evaluated in this paper. The acronyms LS and CL denote the liquid-solid interface (except for the CL region) and CL region, respectively.

| No.	Velocity slip (LS)	Velocity slip (CL)	Contact angle	Note
Solver 1	No slip		Constant value	Native interFoam [44]
Solver 2	Navier slip model		MKT DCA model	Standard method
Solver 3	Navier slip model	MKT slip model	MKT DCA model	Zhang et. al. [26]
Solver 4	Navier slip model		Modified source term	Boelens et. al. [42]
Solver 5	Navier slip model	MKT slip model	Modified source term	Present method

In this section, we use the droplet with an initial radius of 55.8 Å for presentations, and the normalized base radius as well as the instant DCA measured by density contours are used to quantify the dynamic wetting process. The simulation results of MD and

different VOF solvers on the molecular smooth surfaces are shown in Fig. 6. It can be inferred from Fig. 6 that both the base radius and DCA converge to their equilibrium values after a sufficiently long time, indicating that all five solvers can predict the correct equilibrium state of a wetted droplet. However, the dynamic wetting processes predicted by different solvers have obvious distinctions, especially for the early wetting stage ($0 < t^* < 10$). Compared to the benchmark results obtained by MD, the native interFoam solver (Solver 1) significantly underpredicts the temporal evolution of the wetting process. The introduction of the Navier slip and DCA models (Solver 2) enhances the wetting rate to some extent, but it is still far slower than the benchmark results, unless an artificial large slip length is employed in the Navier slip model, as reported in our previous work [26]. The temporal evolution of the normalized base radius and DCA predicted by Solver 4 are quite close to those obtained by Solver 2, confirming that the modified source term derived from the uncompensated Young's stress is qualified to replace the MKT DCA model. However, the performance of Solver 4 at the early stage of dynamic wetting is not further improved, suggesting that the single Navier slip boundary condition for the whole liquid-solid surface is not accurate enough, as the slip mechanism at the three-phase CL region is essentially different and needs to be considered separately. With the MKT slip model plugged into the VOF method for the CL region, both Solver 3 and Solver 5 show good performances throughout the dynamic wetting process. Considering the advantages of replacing DCA models by modifying the momentum equation (cf. the discussion presented in Section 2.1.3), Solver 5, i.e., the one proposed in this work, is considered as the best choice for the simulation of nanodroplets wetting on smooth surfaces among the five implementations.

21
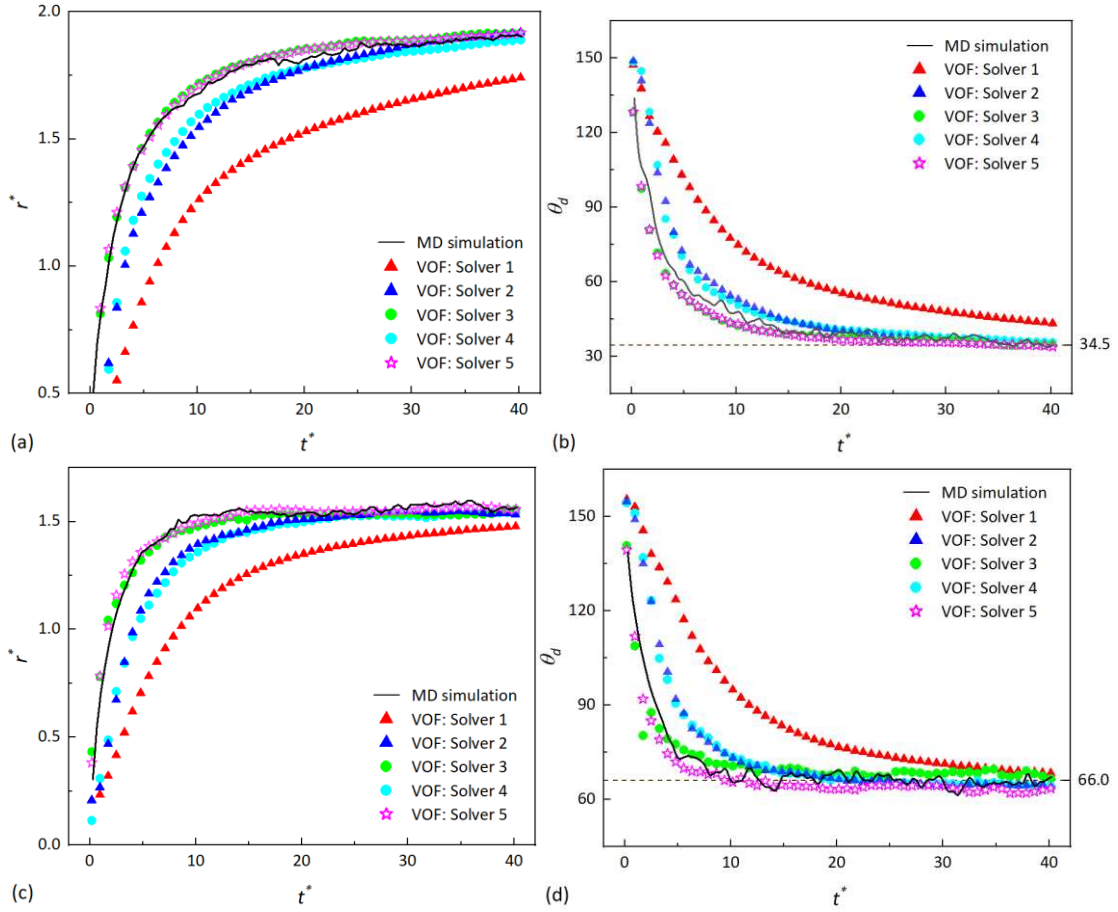
Fig. 6. Temporal evolution of the normalized base radius and DCA of the droplet (r_0=55.8 Å) wetting on the smooth surfaces: (a) normalized base radius, k_ϵ=0.33; (b) DCA, k_ϵ=0.33; (c) normalized base radius, k_ϵ=0.28; (d) DCA, k_ϵ=0.28.

We further evaluate the performance of five solvers on the rough surfaces, which are decorated with concentric annular pillars. Figure 7 shows the snapshots of the last time step simulated by five solvers that the droplet (r_0=55.8 Å) wets on the pillared surface (k_ϵ=0.33). For the sake of comparison, each snapshot comprises the MD result on the left-hand side while the corresponding VOF result is depicted on the right-hand side. It is interesting to see that the droplet morphologies, including the base radius and contact angle obtained by Solvers 1, 2, and 4 are completely different from MD, while Solver 3 seems to give a better prediction and Solver 5 gives the best result.
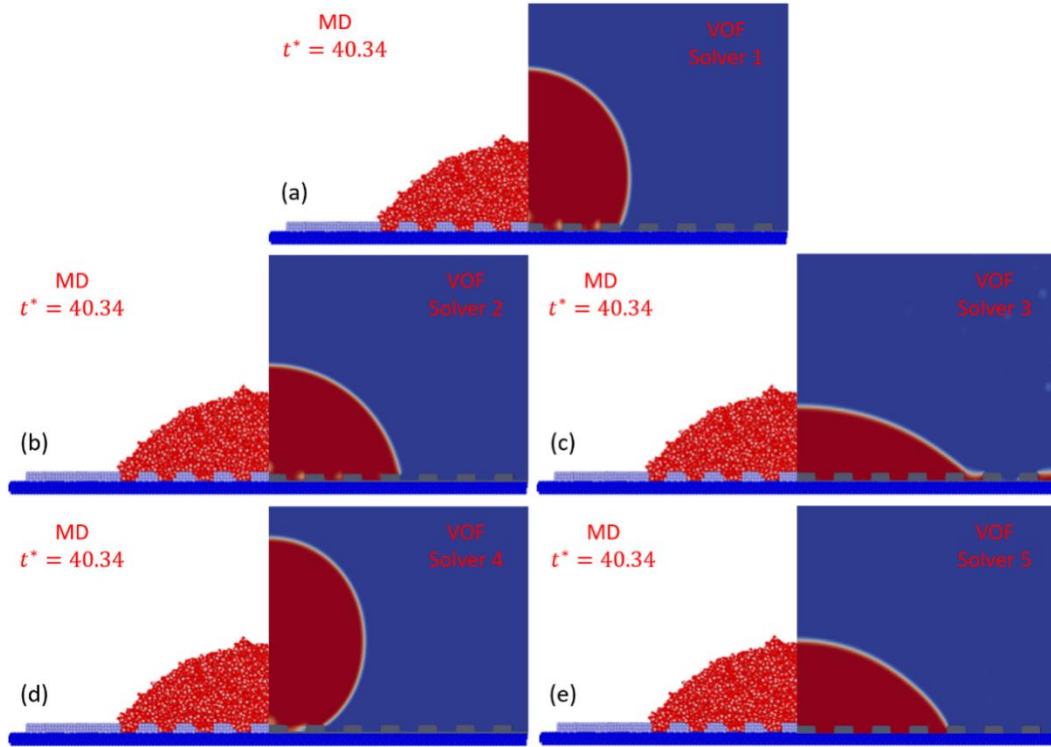
Fig. 7. Cross-sectional snapshots of droplet morphologies when the droplet (r_0=55.8 Å) wets the pillared surface (k_ϵ=0.33) at t^*=40.34. The left side of each subfigure shows the MD result in comparison to the right-side results obtained by different VOF solvers.

The emergence of the pinning-depinning phenomenon on heterogeneous surfaces should be the main cause for the large difference in the simulation performance between five solvers. This phenomenon can be indicated by the step-like temporal variations for both the base radius and contact angle of the droplet predicted by MD, as shown by the black curves in Fig. 8. The molecular origin of this phenomenon lies in the competition of pinning force and depinning force, which are essentially the intermolecular forces exerted on the water molecules in the vicinity of contact line by the solid molecules in pillars and other water molecules in the remaining portion of the droplet, respectively [62]. Considering the contact line advances near the outermost edge of a pillar, it is pinned due to the balance of pinning force and depinning force: as the depinning force increases due to the accumulation of water molecules at the CL region, the pinning force can increase instantaneously by adapting the solid-liquid intermolecular distance,

which is contributed by the bending deformation of pillar structures [62]. The contact line will keep on pinning until the depinning force exceeds the maximum pinning force [63]. Obviously, since the pinning-depinning phenomenon is essentially caused by the intermolecular interactions, MD is able to reproduce it, while its accurate simulation via a VOF model without considering the interfacial molecular physics will be quite more challenging.

As shown in Fig. 8, the dynamic wetting process predicted by Solvers 1, 2, and 4 are much slower than the MD results, indicating that the particular slip mechanism at the CL region is indispensable for the prompt depinning of contact line from the pillar edge. On the contrary, if the MKT slip model is supplemented at the contact line, e.g. Solver 3 and Solver 5, the wetting rate is largely enhanced. The reason for this is that the MKT slip model is derived based on the molecular dynamics, which predicts a non-constant slip velocity for the contact line depending on the molecular movements at the CL region. As the water molecules accumulate in the vicinity of contact line, which is jointly caused by the drive of uncompensated Young's stress and the pinning of contact line, the DCA keeps increasing to make the predicted slip velocity increase as well (cf. Eq. (12)). Consequently, the slip velocity could reach the critical value to get over the maximum pinning force that the pillar molecules can provide, allowing for the prompt depinning of contact line. Compared with the MD results, Solver 5 has a better performance than Solver 3, which should attribute to the dismissal of MKT DCA model that avoids the increasing numerical errors due to the intertwine between it and the MKT slip model, as explained in Section 2.1.3. Overall, the deviations between the dynamic wetting characteristics predicted by Solver 5 and the MD results are within an acceptable level, considering that MD inevitably has statistical noise.

24
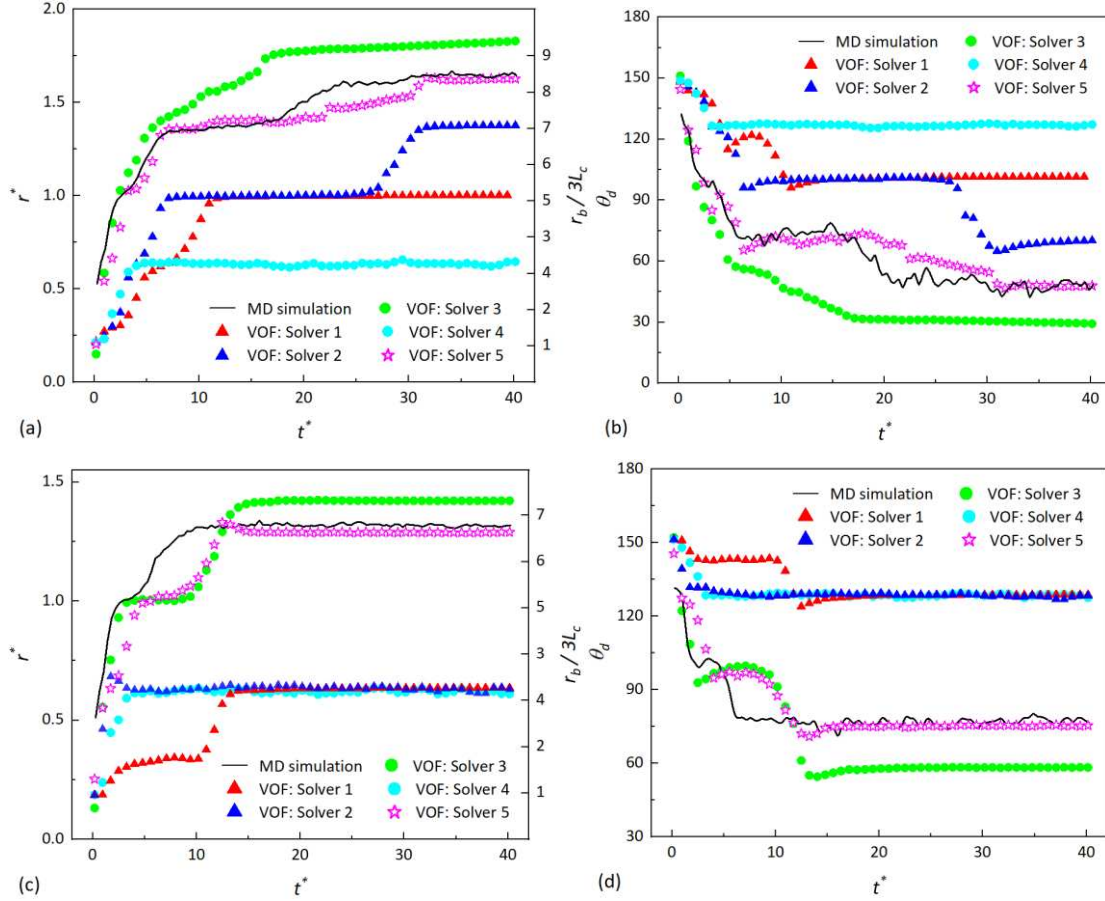
Fig. 8. Temporal evolution of the normalized base radius and DCA of the droplet (r_0=55.8 Å) wetting on the pillared surface: (a) normalized base radius, k_ϵ=0.33; (b) DCA, k_ϵ=0.33; (c) normalized base radius, k_ϵ=0.28; (d) DCA, k_ϵ=0.28.

As a further demonstration, in Fig. 9 we compare the cross-sectional snapshots of a nanodroplet (r_0=55.8 Å) spreading on the pillared surface (k_ϵ=0.33) at several typical instants of time obtained by Solver 5 with those by MD. It can be seen that the overall droplet properties (e.g., radius, height and curvature) obtained by two methods are quite similar. For this case, the computational cost for the MD-VOF multiscale simulation is around eight times less than that for the full MD simulation. With the increase of droplet size, using this kind of multiscale simulation strategy could save more computational resources.
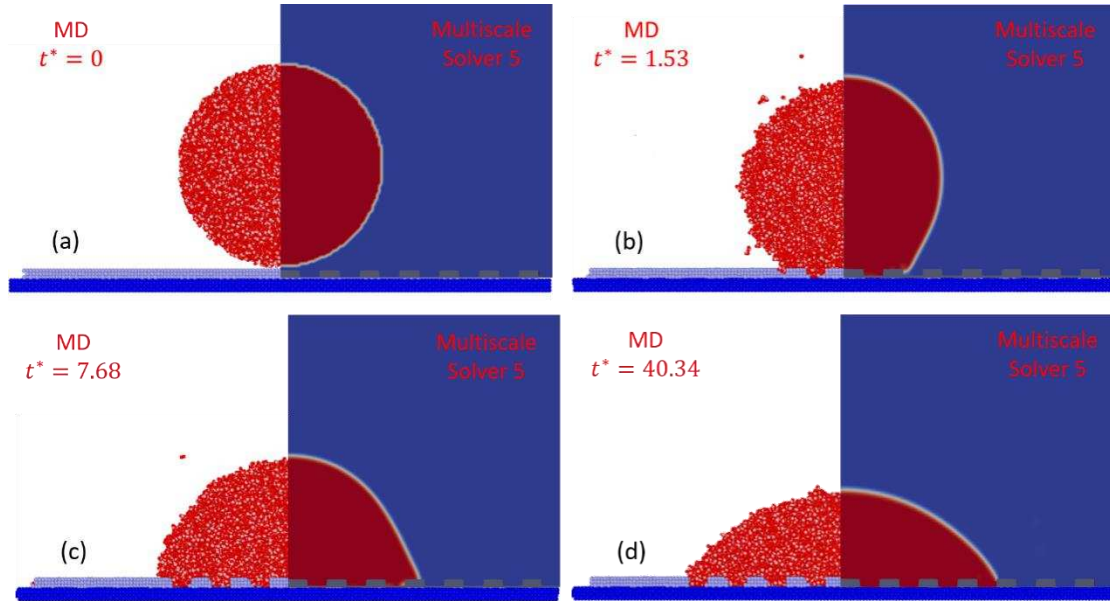
Fig. 9. Comparisons of the cross-sectional snapshots obtained by MD (the left side in each subfigure) and by the multiscale Solver 5 (the right side), at four distinct instants during the droplet (r_0=55.8 Å) wetting on the pillared surface (k_ϵ=0.33).

3.3 Extension of the multiscale simulation method to larger scales.

We have shown that the multiscale method gives good performance on the simulations of dynamic wetting at the nanoscale. To extend its applicability to the larger scales, two critical issues remain to be addressed. One is whether the parameters in VOF boundary conditions obtained by the MD simulations using a certain initial radius of droplet are applicable to simulating droplets of other sizes. To this end, we perform MD simulations of dynamic wetting of droplets with four different initial radii on the smooth surface (k_ϵ=0.33). As shown in Fig. 10, the temporal evolutions of the normalized base radius and DCA both nearly collapse onto one single curve, indicating that they are independent of the droplet size, if the small changes of contact angle due to the effect of line tension is ignored [28]. Therefore, as long as the properties of the droplets and the surfaces are unchanged, the MKT slip boundary condition applied to other cases with different scales can be directly derived with the determined values of

θ_e, θ_d, and r^*_{fit}, as presented in Section 3.1, without resorting to the additional expensive MD simulations.


(a)

(b)
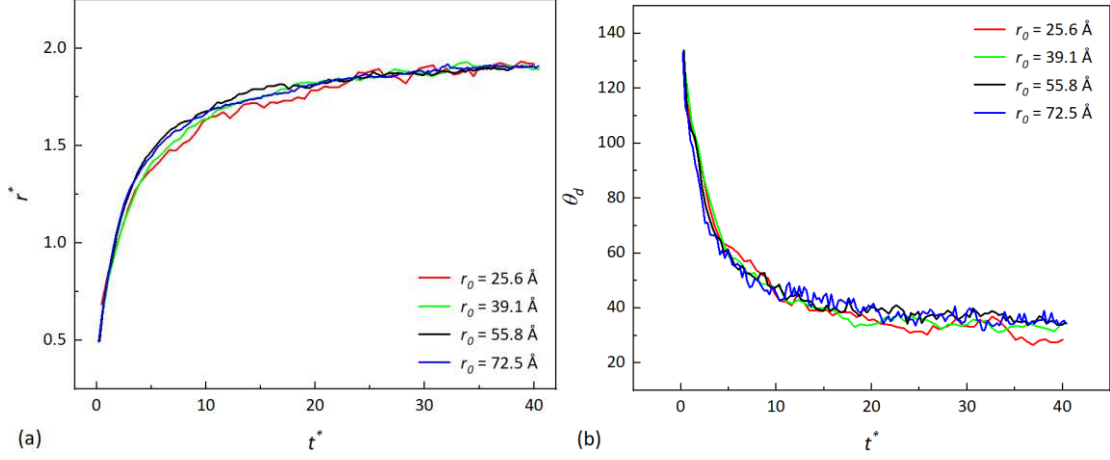
Fig. 10. Temporal evolutions of the (a) normalized base radius and (b) DCA of droplets wetting on the smooth surface (k_ϵ=0.33). The droplets are of four different initial radii.

Another issue is whether the dynamic wetting process predicted by the proposed multiscale method is consistent with those by other VOF methods, for instance, the standard VOF method implemented with the Navier slip and DCA models (Solver 2). To this end, we simulate the wetting process of droplets with initial radii from 55.8 Å to 55.8 μm using Solver 2 and Solver 5. To compare the results obtained by these two solvers, we define a relative error, namely,

$$\delta = \frac{\left|t^*_{2,x} - t^*_{5,x}\right|}{t^*_{2,x}}, \tag{29}$$

where $t^*_{N,x}$ is the normalized time at which the base radius of droplet simulated by Solver N reaches x percent of its maximum value. Specifically, we set x to 50%, 85%, and 98% to characterize the difference of the wetting rate at different wetting stages predicted by Solver 2 and 5. As shown in Fig. 11, this difference at the nanoscale is prominent. On the contrary, the difference above the micrometer scale is down to less than 10%, indicating that our multiscale method is compatible with the standard VOF method at the macroscales, as the effect of the particular slip at the CL region becomes

less important. Note that if the droplet size falls in between nanometer and micrometer, this difference is still notable. Therefore, the present multiscale method essentially provides an efficient approach to simulate the dynamic wetting at such scales, at which MD is limited by the massive computational cost and the standard VOF method is limited by the computational accuracy.
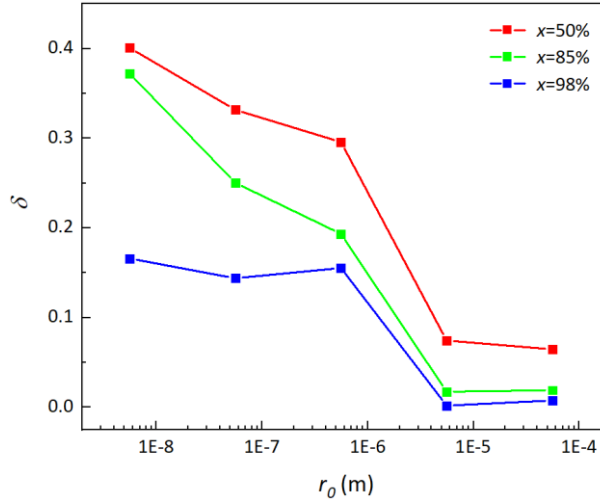
Fig. 11. The relative error of droplet wetting rate simulated by the standard VOF method and present multiscale method.

4. Conclusions

In this paper, we propose a multiscale simulation method for the dynamic wetting problem, based on the recent work of Zhang et. al. (2017) [26] and Boelens et. al. (2019) [42]. Specifically, the volume of fluid (VOF) simulations are enhanced by using the self-consistent boundary conditions derived from molecular dynamics (MD). Different from the standard VOF boundary conditions that employ the Navier slip model for the whole liquid-solid interface and the dynamic contact angle (DCA) models for the variation of contact angle, we include a slip model based on the molecular kinetic theory (MKT) for the three-phase contact line region to account for the particular interfacial molecular physics, as well as the classical Navier slip model for the remaining part of the liquid-solid interface. Besides, a newly-modelled source term that accounts for the

equilibrium effect of the uncompensated Young's stress is supplemented to the momentum equation in VOF to replace the convectional MKT DCA model. The simulation results demonstrate that with these self-consistent boundary conditions, the enhanced VOF simulations can provide consistent predictions with full MD simulations for the dynamic wetting of nanodroplets on both smooth and pillared surfaces. Compared with the standard VOF method and the method of Boelens and de Pablo [42], the multiscale method introduced in this work has significantly better computational accuracy in the prediction of the dynamic wetting of droplets with considerable small sizes, especially on the pillared surfaces where the pinning-depinning phenomenon emerges. Compared with our previous multiscale approach [26], the present method replaces the MKT DCA model by an equivalent source term in the VOF momentum equation, so that the variation of DCA is uncoupled with the calculation of contact line velocity, which is performed by the MKT slip model, to avoid the accumulation of numerical errors. At last, we demonstrate the flexibilities and possibilities of applying this multiscale approach to analogous dynamic wetting problems at larger scales. Considering that the MD is limited by the massive computational cost above the nanoscale, and the standard VOF method is limited by the sensitivity and uncertainty of boundary conditions below the microscale, the present multiscale method provides an efficient and accurate simulation approach for the dynamic wetting at the intermediate scales.

Acknowledgments

References

[1] T. Young, An essay on the cohesion of fluids, Phil. Trans. R. Soc. London **95**, 65 (1805).

[2] J. H. Snoeijer and B. Andreotti, Moving Contact Lines: Scales, Regimes, and Dynamical Transitions, Annu. Rev. Fluid. Mech. **45**, 269 (2013).

[3] S. Kumar, Liquid Transfer in Printing Processes: Liquid Bridges with Moving Contact Lines, Annu. Rev. Fluid. Mech. **47**, 67 (2015).

[4] B. Andreotti and J. H. Snoeijer, Statics and Dynamics of Soft Wetting, Annu. Rev. Fluid. Mech. **52**, 285 (2020).

[5] E. Vandre, M. S. Carvalho, and S. Kumar, On the mechanism of wetting failure during fluid displacement along a moving substrate, Phys. Fluids **25**, 102103 (2013).

[6] V. Bergeron, D. Bonn, J. Y. Martin, and L. Vovelle, Controlling droplet deposition with polymer additives, Nature **405**, 772 (2000).

[7] A. A. Darhuber and S. M. Troian, Principles of Microfluidic Actuation by Modulation of Surface Stresses, Annu. Rev. Fluid. Mech. **37**, 425 (2005).

[8] P. Galliker, J. Schneider, H. Eghlidi, S. Kress, V. Sandoghdar, and D. Poulikakos, Direct printing of nanostructures by electrostatic autofocussing of ink nanodroplets, Nat. Commun. **3**, 890 (2012).

[9] Z. Jian, C. Josserand, S. Popinet, P. Ray, and S. Zaleski, Two mechanisms of droplet splashing on a solid substrate, J. Fluid Mech. **835**, 1065 (2017).

[10] V. Dhir, K., Boiling heat transfer, Annu. Rev. Fluid. Mech. **30**, 365 (1998).

[11] H. Li, W. Fang, Y. Li, Q. Yang, M. Li, Q. Li, X. Q. Feng, and Y. Song, Spontaneous droplets gyrating via asymmetric self-splitting on heterogeneous surfaces, Nat. Commun. **10**, 950 (2019).

[12] M. Sussman, A. S. Almgren, J. B. Bell, P. Colella, L. H. Howell, and M. L. Welcome, An Adaptive Level Set Approach for Incompressible Two-Phase Flows, J. Comput. Phys. **148**, 81 (1999).

[13] C. W. Hirt and B. D. Nichols, Volume of fluid (VOF) method for the dynamics of free boundaries, J. Comput. Phys. **39**, 201 (1981).

[14] S. Manservisi and R. Scardovelli, A variational approach to the contact angle dynamics of spreading droplets, Comput. Fluids **38**, 406 (2009).

[15] M. Renardy, Y. Renardy, and J. Li, Numerical Simulation of Moving Contact Line Problems Using a Volume-of-Fluid Method, J. Comput. Phys. **171**, 243 (2001).

[16] P. R. Gunjal, V. V. Ranade, and R. V. Chaudhari, Dynamics of drop impact on solid surface: Experiments and VOF simulations, AIChE J. **51**, 59 (2005).

[17] S. Arias, D. Legendre, and R. González-Cinca, Numerical simulation of bubble generation in a T-junction, Comput. Fluids **56**, 49 (2012).

[18] S. Li, F. Chu, J. Zhang, D. Brutin, and D. Wen, Droplet jumping induced by coalescence of a moving droplet and a static one: Effect of initial velocity, Chem. Eng. Sci. **211**, 115252 (2020).

[19] C. Huh and L. E. Scriven, Hydrodynamic model of steady movement of a solid/liquid/fluid contact line, J. Colloid Interface Sci. **35**, 85 (1971).

[20] Y. Sui, H. Ding, and P. D. M. Spelt, Numerical Simulations of Flows with Moving Contact Lines, Annu. Rev. Fluid. Mech. **46**, 97 (2014).

[21] D. Jacqmin, Contact-line dynamics of a diffuse fluid interface, J. Fluid Mech. **402**, 57 (2000).

[22] N. Savva and S. Kalliadasis, Dynamics of moving contact lines: A comparison between slip and precursor film models, Europhys. Lett. **94**, 64004 (2011).

[23] Y. D. Shikhmurzaev, Moving contact lines in liquid/liquid/solid systems, J. Fluid Mech. **334**, 211 (1997).

[24] M. N. Popescu, J. Ralston, and R. Sedev, Capillary Rise with Velocity-Dependent Dynamic Contact Angle, Langmuir **24**, 12710 (2008).

[25] A. Ashish Saha and S. K. Mitra, Effect of dynamic contact angle in a volume of fluid (VOF) model for a microfluidic capillary flow, J. Colloid Interface Sci. **339**, 461 (2009).

[26] J. Zhang, M. K. Borg, and J. M. Reese, Multiscale simulation of dynamic wetting, Int. J. Heat Mass Transfer **115**, 886 (2017).

[27] D. C. Rapaport, *The Art of Molecular Dynamics Simulation* (Cambridge University Press, New York, 1995).

[28] J. Zhang, P. F. Wang, M. K. Borg, J. M. Reese, and D. S. Wen, A critical assessment of the line tension determined by the modified Young's equation, Phys. Fluids **30**, 082003 (2018).

[29] J. Fan, J. De Coninck, H. Wu, and F. Wang, Microscopic Origin of Capillary Force Balance at Contact Line, Phys. Rev. Lett. **124**, 125502 (2020).

[30] J. C. Fernández-Toledano, T. D. Blake, J. De Coninck, and M. Kanduč, Hidden microscopic life of the moving contact line of a waterlike liquid, Phys. Rev. Fluids **5**, 104004 (2020).

[31] T. Qian, X. P. Wang, and P. Sheng, Molecular scale contact line hydrodynamics of immiscible flows, Phys. Rev. E **68**, 016306 (2003).

[32] T. Qian, X. P. Wang, and P. Sheng, Power-law slip profile of the moving contact line in two-phase immiscible flows, Phys. Rev. Lett. **93**, 094501 (2004).

[33] W. Ren and W. E, Boundary conditions for the moving contact line problem, Phys.

Fluids **19**, 022101 (2007).

[34] J. J. Shu, J. B. Teo, and W. K. Chan, A new model for fluid velocity slip on a solid surface, Soft Matter **12**, 8388 (2016).

[35] A. V. Lukyanov and T. Pryer, Hydrodynamics of Moving Contact Lines: Macroscopic versus Microscopic, Langmuir **33**, 8582 (2017).

[36] Z.-X. Tong, Y.-L. He, and W.-Q. Tao, A review of current progress in multiscale simulations for fluid flow and heat transfer problems: The frameworks, coupling techniques and future perspectives, Int. J. Heat Mass Transfer **137**, 1263 (2019).

[37] H. F. Wu, K. A. Fichthorn, and A. Borhan, An atomistic–continuum hybrid scheme for numerical simulation of droplet spreading on a solid surface, Heat Mass Transf. **50**, 351 (2013).

[38] M. E. Kavousanakis, C. E. Colosqui, I. G. Kevrekidis, and A. G. Papathanasiou, Mechanisms of wetting transitions on patterned surfaces: continuum and mesoscopic analysis, Soft Matter **8** (2012).

[39] S. F. Kistler, *Hydrodynamics of wetting,* in *Wettability*, edited by J. Berg (Marcel Dekker, New York, 1993), p. 311.

[40] Y. D. Shikhmurzaev, The moving contact line on a smooth solid surface, Int. J. Multiphase Flow **19**, 589 (1993).

[41] S. Kalliadasis and H. C. Chang, Apparent dynamic contact angle of an advancing gas–liquid meniscus, Phys. Fluids **6**, 12 (1994).

[42] A. M. P. Boelens and J. J. de Pablo, Generalised Navier boundary condition for a volume of fluid approach using a finite-volume method, Phys. Fluids **31**, 021203 (2019).

[43] H. G. Weller, G. Tabor, H. Jasak, and C. Fureby, A tensorial approach to computational continuum mechanics using object-oriented techniques, Comput. Phys.

12, 620 (1998).

[44] O. Ubbink, Numerical prediction of two fluid systems with sharp interfaces, Ph.D. thesis, Imperial College London (1997).

[45] S. S. Deshpande, L. Anumolu, and M. F. Trujillo, Evaluating the performance of the two-phase flow solver interFoam, Comput. Sci. Discov. **5**, 014016 (2012).

[46] J. U. Brackbill, D. B. Kothe, and C. Zemach, A continuum method for modeling surface tension, J. Comput. Phys. **100**, 335 (1992).

[47] I. Malgarinos, N. Nikolopoulos, M. Marengo, C. Antonini, and M. Gavaises, VOF simulations of the contact angle dynamics during the drop spreading: standard models and a new wetting force model, Adv. Colloid Interface Sci. **212**, 1 (2014).

[48] K. Mahady, S. Afkhami, and L. Kondic, A volume of fluid method for simulating fluid/fluid interfaces in contact with solid boundaries, J. Comput. Phys. **294**, 243 (2015).

[49] R. S. Voronov, D. V. Papavassiliou, and L. L. Lee, Boundary slip and wetting properties of interfaces: correlation of the contact angle with the slip length, J. Chem. Phys. **124**, 204701 (2006).

[50] S. B. Ramisetti, M. K. Borg, D. A. Lockerby, and J. M. Reese, Liquid slip over gas nanofilms, Phys. Rev. Fluids **2** (2017).

[51] T. D. Blake and J. M. Haynes, Kinetics of liquid/liquid displacement, J. Colloid Interface Sci. **30**, 421 (1969).

[52] M. J. de Ruijter, T. D. Blake, and J. De Coninck, Dynamic Wetting Studied by Molecular Modeling Simulations of Droplet Spreading, Langmuir **15**, 7836 (1999).

[53] See Supplemental Material at [URL] for the discussion on the modification function h(α).

[54] S. Plimpton, Fast Parallel Algorithms for Short-Range Molecular Dynamics, J.

Comput. Phys. **117**, 1 (1995).

[55] A. Stukowski, Visualization and analysis of atomistic simulation data with OVITO – the Open Visualization Tool, Modelling Simul. Mater. Sci. Eng. **18**, 015012 (2009).

[56] H. Liu, F. Chu, J. Zhang, and D. Wen, Nanodroplets impact on surfaces decorated with ridges, Phys. Rev. Fluids **5**, 074201 (2020).

[57] J. L. F. Abascala and C. Vega, A general purpose model for the condensed phases of water: TIP4P/2005, J. Chem. Phys. **123**, 234505 (2005).

[58] H. C. Andersen, Rattle: A "velocity" version of the shake algorithm for molecular dynamics calculations, J. Comput. Phys. **52**, 24 (1983).

[59] Amar and G. Jacques, Effects of long-range interactions in metal epitaxial growth, Phys. Rev. B **67**, 286 (2003).

[60] J. Zhang, M. K. Borg, K. Sefiane, and J. M. Reese, Wetting and evaporation of salt-water nanodroplets: A molecular dynamics investigation, Phys. Rev. E **92**, 052403 (2015).

[61] E. Bertrand, T. D. Blake, and J. D. Coninck, Influence of solid-liquid interactions on dynamic wetting: a molecular dynamics study, J Phys Condens Matter **21**, 464124 (2009).

[62] F. Wang and H. Wu, Molecular origin of contact line stick-slip motion during droplet evaporation, Sci Rep **5**, 17521 (2015).

[63] D. Bonn, J. Eggers, J. Indekeu, J. Meunier, and E. Rolley, Wetting and spreading, Rev. Mod. Phys. **81**, 739 (2009).